

Controlling exciton dynamics in two-dimensional MoS₂ on hyperbolic metamaterial-based nanophotonic platform

Kwang Jin Lee^{1,5}, Wei Xin^{2,5}, Chunhao Fann¹, Xinli Ma³, Fei Xing⁴, Jing Liu³, Jihua Zhang¹, Mohamed Elkabbash¹, Chunlei Guo^{1,2*}

¹ Institute of Optics, University of Rochester, Rochester, New York, USA,

² The Guo China-US Photonics Laboratory, Changchun Institute of Optics, Fine Mechanics and Physics, Chinese Academy of Sciences, Changchun, China, 130033

³ State Key Laboratory of Precision Measurement Technology and Instruments, School of Precision Instruments and Opto-electronics Engineering, Tianjin University, Tianjin, China, 300072

⁴ School of Physics and Optoelectronic Engineering, Shandong University of Technology, Zibo, China, 255049

⁵ These authors contributed equally to this work

*e-mail: guo@optics.rochester.edu

The discovery of two-dimensional transition metal dichalcogenides (2D TMDs) has promised next-generation photonics and optoelectronics applications, particularly in the realm of nanophotonics. Arguably, the most crucial fundamental processes in these applications are the exciton migration and charge transfer in 2D TMDs. However, exciton dynamics in 2D TMDs have never been studied on a nanophotonic platform and more importantly, the control of exciton dynamics by means of nanophotonic structures has yet to be explored. Here, for the first time, we demonstrate the control of exciton dynamics in MoS₂ monolayers by introducing a hyperbolic metamaterial (HMM) substrate. We reveal the migration mechanisms of various excitons in MoS₂ monolayers. Furthermore, we demonstrate the Förster radius of the A-excitons can be increased by introducing HMMs through the nonlocal effects of HMMs due to the Purcell effect. On the other hand, the diffusion coefficient is unchanged for the C-excitons on HMMs. This study provides a revolutionary step forward in enabling 2D TMD nanophotonics hybrid devices.

With the explosive research activities since the discovery of graphene, two-dimensional (2D) materials have emerged as one of the most exciting areas studied in science and engineering¹⁻⁵. Among them, 2D transition metal dichalcogenides (TMDs) have attracted a great amount of attentions and been considered as an ideal material for nanophotonic and optoelectronic applications due to their remarkable optical and electronic properties, such as, higher photoluminescence efficiency due to direct bandgap and existence of light-valley interactions⁶⁻¹¹. Atomically-thin monolayer TMDs have strongly bounded excitons because of the enhancement in quantum confinement and Coulomb interactions, and this strong bonding dominates most optical and electronic effects. In general, exciton binding energy in TMD monolayers is an order of magnitude higher than that of previously investigated 2D quantum well structures, which leads to their unique optoelectronic characteristics and makes TMDs an ideal platform for exploring exciton dynamics (ED) that is essential for photo-current conversion processes and novel optoelectronic applications^{12,13}. An analogue can be seen in organic semiconductors, which also have large exciton binding energies due to their low dielectric constants and this effect incites a large amount of exciton dynamics studies in organic photovoltaic operation¹⁴⁻¹⁷. Therefore, a thorough characterization of ED is of paramount importance for improving light-harvesting applications as well as revealing fundamental mechanism of carrier dynamics in 2D TMD materials. Furthermore, understanding and controlling ED in these materials when integrated into a nanophotonic platform has never been explored before.

Engineering light-matter interactions has been realized using nanophotonic structures, e.g., metamaterials and engineered materials with tailored optical properties¹⁸⁻²⁰. Particularly, metamaterials have been used in optoelectronic devices^{21,22}, optical sensing²³, plasmonic lasers²⁴ and Raman spectroscopy²⁵. Among various types of metamaterials, hyperbolic metamaterials (HMMs) have been extensively studied over the past few years due to their unusual optical properties from the high- k states²⁶⁻³⁰. HMM structures that have been shown to exert nonlocal effects on the photophysical properties of their surrounding environment have recently been reported^{31,32}, which suggests that TMDs can be drastically altered without modifying the material itself, but instead by incorporating a TMD on a HMM.

MoS₂ monolayers exhibit two typical band-edge excitons, A- and B-excitons, resulting from transitions between the conduction band minimum and spin-orbit split valence band maximum near the K point. In addition, recent studies observed another exciton, labelled as C-excitons, with a strong and broadband absorption at higher energies. C-exciton states are attributed to the band nesting effect, i.e., transition arising from the maxima in the joint density of state (JDOS) when the conduction and valence bands are parallel in a region between K and Γ points³³⁻³⁷. Unlike A- and B-excitons, C-excitons have no photoluminescence. Although a few studies have attempted to address some aspects of ED in TMD monolayers³⁸⁻⁴⁰, the underlying mechanism still remains unclear. Particularly, the ED in TMD monolayers has never been studied on a nanophotonic platform.

In this article, we study comprehensively the nonlocal effect of HMMs on ED in MoS₂ monolayers. We show that ED in the A and C-excitons have very different dynamics; the migration of A- excitons is mainly through a single-step Förster-type resonance energy transfer (FRET) whereas multi-step diffusion process is responsible for C-excitons. We also find that the Förster radius increases in the presence of the HMM substrates in the hyperbolic dispersion region, but the diffusion constant is not affected by the HMMs. We elucidate that the increased Förster radius comes from the nonlocal effects of HMMs from the Purcell effect. We note there has been ongoing debates in understanding FRET in complex photonic environment⁴¹, and this study provides conclusive evidence to address these issues.

Sample configuration and transient absorption measurement

MoS₂ monolayer was prepared on silicon substrates by means of chemical vapor deposition. Single-layer samples were identified by optical microscopy and Raman spectra shown in SI-figure 1. Multi-layered HMMs consisting of 5 pairs of alternative Ag-TiO₂ layers with different fill factors ($f=0.2, 0.5$ and 0.8) were fabricated by electron beam evaporation. Detail sample configurations are described in SI-figure 2. We confirmed that the peaks of Raman spectra were not altered with HMM substrates (SI-Figure 3). In our design, a 10-nm thick Al₂O₃ layer was deposited on top of the stack to avoid the convolution of other processes such as charge transport between MoS₂ and HMMs. (Band alignments are illustrated in SI-figure 4). Figure 1a schematically displays the sample configuration for MoS₂ monolayer deposited on a HMM structure with $f = 0.5$ (10 nm thickness of each layer). To observe the ED, we used exciton-exciton annihilation (EEA) method by performing ultrafast transient absorption (TA) experiment based on the pump-probe technique described below. Figure 1b shows the absorption and photoluminescence spectra of MoS₂ monolayer. The two absorption peaks at 1.87 eV and 2.05 eV correspond to A- and B-excitons of MoS₂ monolayers, respectively. The broad absorption band above 2.8 eV corresponds to the non-emissive C-excitons. The photoluminescence peak and shoulder at 1.84 eV and 2.01 eV correspond to A- and B-excitons, respectively. Figure 1c presents the real part of an effective dielectric constant of HMMs along the transverse direction calculated by effective medium theory. HMM with $f = 0.8$ ($f = 0.2$) shows hyperbolic (elliptic) dispersions region for both A- and C-excitons, whereas HMM with $f = 0.5$ exhibits hyperbolic (elliptic) dispersion for A- (C-) excitons.

Exciton dynamics for A- and C-excitons

Ultrafast TA experiments were carried out to analyze the ED of MoS₂ monolayers by measuring relative reflection ($\Delta R/R$). The pump beam at 2.25 eV (3.05 eV) and probe beam at 1.85 eV (3.05 eV) were chosen

for A- (C-) excitons. The pump fluence for A- and C-excitons were adjusted to obtain the same initial exciton densities (n_0) immediately after the excitation by the pump. (SI-figure 5) Figures 2a and 2b show the normalized TA kinetics of A- and C-excitons in MoS₂ monolayer on Si substrate without metamaterials for different exciton densities. At the lowest initial exciton density ($n_0=0.06 \times 10^{12} \text{ cm}^{-2}$), TA kinetics for both A- and C-excitons are fitted by a mono-exponential decay functions with characteristic time (τ) of about 186 ps and 213 ps, corresponding to the intrinsic exciton lifetimes. C-excitons have a relatively longer lifetime than A-excitons, and this is consistent with previous works, which show that favorable band alignment and transient excited state Coulomb environment could lead to a longer lifetime of C-excitons^{33,36}. As n_0 increases, the decay of A-excitons deviates from a mono-exponential fitting due to an EEA taking place where two excitons are sufficiently close to interact and to generate a single exciton with a higher energy. Using bi-exponential decay fitting, we found that the short time constant (τ_1) decreases with n_0 . On the other hand, the longer time constant (τ_2) is almost independent of n_0 , indicating that τ_1 represents EEA phenomenon and τ_2 corresponds to the intrinsic exciton lifetime (SI-figure 6). For C-exciton, we observed a relatively weak dependence on n_0 , which is also consistent with previous work suggesting that the exciton dissociation occurs efficiently, in agreement with the self-separation of photocarriers in the nesting region in the momentum space³⁷. In addition, for A-excitons, we note that figure 2a is consistent with previous study.³⁸

Figures 2c and 2d display the TA decays for A- and C-excitons in the initial time range (up to ~ 100 ps). To analyze the EEA behaviour, we consider the rate equation of EEA described by^{42,43}

$$\frac{d}{dt}n(t) = -\frac{n(t)}{\tau} - \frac{1}{2}\gamma(t)n(t)^2 \quad (1)$$

where $n(t)$ is the exciton density at a delay time t after the excitation, $\gamma(t)$ is the annihilation rate coefficient and τ is the exciton lifetime at the low exciton density limit (τ_2). The factor 1/2 represents that only one exciton is left after EEA. We note that EEA is dominant over the Auger recombination in this structure³⁵. In general, EEA process can be classified by three different mechanisms: three-dimensional (3D) and one-dimensional (1D) multi-step exciton diffusions and a single-step FRET⁴². The exciton diffusion model assumes that the excitons move in random walk in many steps towards each other before the annihilation takes place. On the other hand, FRET model considers that annihilation occurs directly via long-range energy transfer processes (SI-Figure 7). FRET strongly depends on the overlap between the emission spectrum of the donor and the absorption spectrum of the acceptor.

For 2D MoS₂ monolayers, we only need to consider FRET and 1D exciton diffusion mechanisms. $\gamma(t)$ is given by $\alpha t^{-1/2}$ where $\alpha=R_F^2\pi^{3/2}/2\tau^{1/2}$ for the FRET model with R_F is the Förster radius and $\alpha=(8D/\pi)^{1/2}/aN_0$ for the 1D diffusion model with the diffusion constant D , lattice constant a and molecular density N_0 . From these relations, Eq. (1) can be solved as^{42,43},

$$n(t) = \frac{n_0 e^{-t/\tau}}{1 + \beta \operatorname{erf}\left(\sqrt{\frac{t}{\tau}}\right)} \quad (2)$$

where ‘erf’ is the error function. The coefficient β is expressed by $n_0 R_F^2 \pi^2 / 4$ and $n_0 l_D / a N_0$ for FRET and the 1D diffusion process, respectively. l_D is the diffusion length defined as $(2D\tau)^{1/2}$. The a and N_0 of MoS₂ monolayers were taken as 3.16 Å and $5.7 \times 10^{14} \text{ cm}^{-2}$, respectively. Here, it is worth noting that $n(t)$ for both the FRET and 1D exciton diffusion models have the same mathematical structure.

The solid curves in figures 2b and 2e represent the fits based on Eq. (2). For C-excitons, FRET was excluded due to their non-emissive property.⁴² The diffusion constant D determined from the fits of the TA decays based on the 1D diffusion model is plotted in figure 2f. Here, the exciton lifetime τ without

annihilation was kept as a constant ($\tau = 213$ ps) and thus was not a fitting parameter. For the highest value of D , we can also estimate l_D as ~ 88 nm, which is considerably longer than that for organic semiconductors and polymers as shown in SI-Figure 8. To better understand the diffusion mechanism, we plot D versus the inverse of square root of the pump fluence that corresponds to the inverse square root of temperature ($T^{-1/2}$) in SI-Figure 9. The linear behaviour of D with $T^{-1/2}$ indicates that the diffusion process takes place through phonon scattering^{43,44}.

Due to the strong overlap between the absorption and emission spectra of A-excitons, annihilation via FRET is likely to dominate the EEA process. Figure 2e shows R_F as a function of n_0 for A-exciton. We find that R_F value is around 6.0 ~ 6.4 nm and hardly depends on n_0 , which is consistent with the fact that exciton density is not related to R_F . Since FRET is not a prerequisite for A-exciton emission, we can consider the diffusion process as the exclusive mechanism for A-excitons. However, when we plot D instead of R_F as shown in SI-Figure 10, we noticed D does not depend on n_0 , indicating that diffusion is not the main mechanism for A-excitons.

Effect of hyperbolic metamaterials

Figure 3 shows the behavior of time constants with different substrates. We note that τ_1 and τ_2 remain constant for all substrates with no overlapping hyperbolic dispersion, while a discernible decrease in τ_1 and τ_2 is observed for HMM with $f=0.5$ and 0.8 . of the decrease of τ_2 from 186 ps to 150 ps can be easily understood in terms of the Purcell factor (PF) enhancement based on the high local density of optical states provided by HMMs. Here, we obtain PF of ~ 1.24 from basic relationship given by $\tau_2^{\text{Si}}/\tau_2^{\text{HMM}}$. (SI-Table 1) Interestingly, a shortening of τ_1 due to the hyperbolic dispersion indicates that the nonlocal effect of HMM based on the PF enhancement clearly affect ED occurring through FRET. The 1p substrate consists of a single pair of 10 nm thick Ag/TiO₂ films with a 10-nm Al₂O₃ serves as a control sample showing the relatively unmodified decay kinetics of MoS₂. For C-excitons, while τ_1 appears to be independent of the substrates, we observed an increase in τ_2 within experimental error. The increase in τ_2 is somewhat similar to the increase in the charge recombination time with the HMM substrates observed in previous studies³¹. The entire TA data were plotted in SI-Figure 11. In SI-Figure 12, we adjusted pump fluence to obtain the same n_0 by considering field intensity variation in the presence of HMM structures so that we could exclude additional effects that can affect n_0 .

In figures 4a and 4b, we plot R_F and D as functions of n_0 for Si and HMM with $f=0.2$ and 0.8 substrates, respectively. We can see that HMM with $f=0.5$ is almost identical to $f=0.8$. Figure 4a exhibits an enhancement in R_F for the A-excitons in the HMM hyperbolic dispersion regimes. We can explain this interesting result in terms of the nonlocal effect of HMMs based on the PF enhancement, which was shown previously that the nonlocal effect of HMMs could lead to a decrease in the refractive index of the environment³². Here, we equivalent the problem as the emitter was placed in a homogenous medium with modified n . Based on this discussion, we showed that PF is inversely proportional to n^3 (Method). We also apply this concept to FRET, and we obtained the relationship between R_F and PF (denoted as F_p) as follows, (Method section).

$$R_F \propto F_p^{\frac{2}{9}} \quad (3)$$

This relation presents a quantitative enhancement factor R_F by 1.05, which is displayed as the open circles in figure 4a. Surprisingly, the predicted values based on the nonlocal effect of HMMs are almost consistent with the experimental values. We note that the current MoS₂-HMM hybrid systems are an ideal platform to investigate the fundamental relationship between FRET and photonic environment by excluding quenching effects such as donor-HMM coupling and the charge transport between MoS₂ and HMMs. In case of the diffusion processes, as shown in figure 4b, there is no noticeable change in the presence of HMMs, which can be explained by the fact that diffusion processes are not relevant for light-matter interactions. Figure 4c illustrates the overall ED for both A- and C-excitons in MoS₂ monolayers.

Conclusion and Discussion

In conclusion, we reveal the different underlying mechanisms for ED in MoS₂ monolayers for the first time such that a single-step Förster-type resonance energy transfer is predominant for A-excitons while a multi-step diffusive motion is responsible for C-excitons. Furthermore, we provide TMDs with a range of nanophotonic platforms using HMMs with different fill factors and find an increase in the Förster radius for A-excitons when A-exciton spectral region lies in the hyperbolic dispersion region. The consistency between experimental results and theoretical rationalization in terms of the nonlocal effect of HMMs based on the Purcell effect shows a decisive evidence that HMMs can alter the FRET efficiency. Our study not only identifies the exact physical mechanisms for ED in MoS₂ monolayers, but also provides a conceptual basis for how FRET is affected by HMM structures. Fundamentally, ED and FRET play vital roles in a broad range of technological fields, such as material science, nanophotonics, biology, and optoelectronics. Technologically, our work demonstrates a novel way to nano-engineering 2D materials with a metamaterial-based nanophotonic platform, which will advance the applications of 2D materials in photonics, optoelectronics, and meta-devices.

Method

Sample preparation

The preparation of a single-layer MoS₂ on silicon substrate (<100>, ≈300 nm SiO₂) is based on traditional chemical vapor deposition (CVD) method (high temperature, Argon environment for 2.5 h). MoO₃ (99.99%, Aladdin) and S (99.99%, Alfa Aesar) powders were chosen as precursor materials. The PTAS (perylene-3, 4, 9, 10-tetracarboxylic acid tetra potassium salt) was also dropped on the substrate as the seeding promoter to increase the nucleation. After that, by using the wet transfer method, the CVD single-layer MoS₂ was then transferred onto the target hyperbolic metamaterials (HMM) that consists of Al₂O₃ film, multi-layered Ag-TiO₂ layers, and silica substrate. To remove the surface contaminants and make a close contact between MoS₂ and the substrate, annealing at 300 °C for 1 h was used.

Absorption, Photoluminescence and Raman spectra measurement

The UV–vis absorption of CVD single-layer MoS₂ on silica and HMM substrates were both carried out using a Cary 5000 UV–visible–NIR spectrometer (Agilent). The Raman and photoluminescence signals were collected by a LabRAM HR Evolution Raman spectrometer (Horiba Jobin Yvon, 100× objective (N.A. = 0.9) and 1800 lines mm⁻¹ gratings). The excitation laser was 532 nm at a power of 0.1 mW.

Transient absorption measurement

Ultrafast transient absorption measurements were carried out using a femtosecond pump-probe setup. A Ti:sapphire regenerative amplifier system is used that delivers 2 μJ pulses at 67-fs in duration, with a wavelength centered at 800 nm (1.55 eV) and a repetition rate of 1 kHz. The laser output is split into a pump and a probe beam by a beam splitter. For the A-exciton measurements, the pump and probe beams were obtained by each passing through a 5-mm thick sapphire window to generate white-light-continuum, followed by further passing through a band-pass filter centered at 2.25 eV for the pump and 1.85 eV for the probe. Each bandpass filter has a bandwidth of 0.03 eV. For the C-exciton measurements, second harmonic (3.05 eV) is generated from the fundamental laser beam using a BBO crystal and the beam is further split into a pump and a probe. The Pump beam was modulated using a mechanical chopper at 220 Hz and the relative reflection $\Delta R/R$ of the probe beam as a function of the delay time was further read out with a photodiode and a lock-in amplifier. The relative reflectance is given by $\Delta R/R = (R_{on} - R_{off})/R_{off}$, where R_{on} and R_{off} are the sample reflectance with the pump beam on and off, respectively. The beam sizes of the pump and probe beams are 100 μm and 80 μm in diameter, respectively. The pump power was varied using variable neutral density filters.

Calculation of exciton density

The initial excitation density (n_0) immediately after the pump excitation can be calculated by the following equation⁴³,

$$n_0 = \frac{f(1-10^{-A})}{E_{\text{pump}}} \quad (\text{M1})$$

where f is the pump fluence, E_{pump} is the photon energy of pump beam and A is the absorbance for a given energy given by absorption coefficient times layer thickness.

Derivation of $\gamma_F(t)$ for two-dimensional case

To derive a rate equation for a single-step annihilation mechanism through FRET, we started with the trapping problem based on the Förster model where a donor molecule is surrounded by acceptor molecules with the volume concentration n_T . In this case, the final decay rate of a single donor molecule can be represented by a summation of the intrinsic decay rate and the energy transfer rates between a single donor molecule to all the surrounding acceptor molecules. Hence, we can obtain the time dependent exciton density on the donor molecules by averaging over all distributions of donor molecules as following⁴²

$$n(t) = n_0 \cdot \exp\left(-\frac{t}{\tau} - \alpha \cdot n_T \sqrt{\frac{\pi t}{\tau}}\right) \quad (\text{M2})$$

Depending on the dimensionality, coefficient α is given by

$$\alpha_{3D} = \frac{4}{3} \pi R_F^3, \quad \alpha_{2D} = \pi R_F^2 \quad (\text{M3})$$

α_{3D} and α_{2D} are the total volume and area at which FRET can take place for three- and two-dimension, respectively. In this work, we adopt α_{2D} considering the current system we are dealing with is a two-dimensional monolayer.

Derivation of $n(t)$ with respect to t yields a rate equation as following

$$\frac{d}{dt} n(t) = -\frac{n(t)}{\tau} - \gamma_F(t) n_T n(t) \quad (\text{M4})$$

where the exciton annihilation rate $\gamma(t)$ is defined as

$$\gamma_F(t) = \frac{1}{2} \pi R_F^2 \sqrt{\frac{\pi}{\tau t}} \quad (\text{M5})$$

Förster radius

Förster radius is generally expressed as

$$R_F^6 = \frac{9\eta_D \kappa^2}{128\pi^5 n^4} \int d\lambda \lambda^4 F_D(\lambda) \sigma_A(\lambda) \quad (\text{M6})$$

where κ is the dipole orientation factor, n is the refraction index of the environment, λ is the wavelength, F_D is the normalized emission spectrum, and σ_A is the absorption cross-section. η_D is the quantum yield expressed as the ratio of the rate of radiative recombination to the total rate of exciton decay. We note that η_D , F_D and σ_A are the individual properties for isolated configuration so that the above equation is not associated with the density of donor and acceptor.

Relationship between Purcell factor and Förster radius

When an emitter is located at a distance of d away from a metallic film with a perpendicular or parallel orientation to the interfaces, the Purcell factors can be written as²⁸,

$$F_{\text{perp}} = 1 - \eta + \frac{3}{2} \eta \text{Re} \int_0^\infty dk_x \frac{1}{k_z} \left(\frac{k_x}{k_0} \right)^3 \frac{1}{n^3} \left[1 + r_p e^{2ik_z d} \right]$$

$$F_{\text{para}} = 1 - \eta + \frac{3}{4} \eta \text{Re} \int_0^\infty dk_x \frac{1}{n k_0 k_z} \left(1 + r_s e^{2ik_z d} + \frac{k_x}{n^2 k_0^2} \left[1 - r_p e^{2ik_z d} \right] \right) \quad (\text{M7})$$

where η is the internal quantum efficiency of the emitters in a free space; k_x (k_z) is the component of the wavevector along the x (z) axis, and k_0 is the magnitude of the wavevector in vacuum; r_p and r_s is the reflection coefficient at the interfaces for p- and s-polarized waves, respectively. In the presence of HMMs, both k and r should be altered so that Purcell factor can be enhanced. In this study, we assume that the emitter is located in a homogeneous medium with a nonlocally modified refractive index, taking into account the overall alteration of k and r by the HMMs. Therefore, we can write the Purcell factor as follows:

$$F_{\text{perp}} = \frac{3}{2} \text{Re} \int_0^\infty dk_x \frac{1}{k_z} \left(\frac{k_x}{k_0} \right)^3 \frac{1}{n_{\text{HMM}}^3}$$

$$F_{\text{para}} = \frac{3}{4} \text{Re} \int_0^\infty dk_x \frac{1}{n_{\text{HMM}} k_0 k_z} \left(1 + \frac{k_z^2}{n_{\text{HMM}}^2 k_0^2} \right) \quad (\text{M8})$$

where η is assumed to be unity and n_{HMM} is the nonlocal refractive index by taking into account the impact of the HMM substrate on k_0 , k_x , and k_z . Also, r_p and r_s are zero because we assume that the emitter is placed in a uniform media with refractive index n_{HMM} . Hence, we can obtain the following relation between the Purcell factor and n_{HMM} ,

$$F_p^{\text{HMM}} \propto n_{\text{HMM}}^{-3} \quad (\text{M9})$$

This relationship shows that the Purcell factor enhancement leads to a decrease in nonlocal refractive index. The above equation can be rewritten as

$$n_{\text{HMM}} \propto \left(F_p^{\text{HMM}} \right)^{-\frac{1}{3}} \quad (\text{M10})$$

We can reconsider Eq.(M6) to extract the relationship between nonlocal refractive index and the Förster radius. In the presence of HMMs, we can also consider the physically equivalent homogeneous configuration with nonlocally modified refractive index n_{HMM}

$$R_F^{\text{HMM}} = \alpha (n_{\text{HMM}})^{-\frac{2}{3}} \quad (\text{M11})$$

where

$$\alpha = \left(\frac{9\eta_D \kappa^2}{128\pi^5} \int d\lambda \lambda^4 F_D(\lambda) \sigma_A(\lambda) \right)^{\frac{1}{6}} \quad (\text{M12})$$

Based on Eq. (M10) and (M11), we can obtain the final relationship between nonlocal refractive index and the Förster radius as following

$$R_F^{\text{HMM}} \propto (F_p^{\text{HMM}})^{\frac{2}{9}} \quad (\text{M13})$$

Reference

1. Geim, A. K. & Novoselov, K. S. The rise of graphene. *Nature Mater.* **6**, 183–191 (2007).
2. Bonaccorso, F., Sun, Z., Hasan, T. & Ferrari, A. C. Graphene photonics and optoelectronics. *Nat. Photonics* **4**, 611–622 (2010).
3. Butler, S. Z. *et al.* Progress, challenges, and opportunities in two-dimensional materials beyond graphene. *ACS Nano* **7**, 2898–2926 (2013).
4. Wang, Q. H., Kalantar-Zadeh, K., Kis, A., Coleman, J. N. & Strano, M. S. Electronics and optoelectronics of two dimensional transition metal dichalcogenides. *Nat. Nanotechnol.* **7**, 699–712 (2012).
5. Xin Wei *et al.*, Black-Phosphorus-Based Orientation-Induced Diodes, *Adv. Mater.* **30**, 1704653 (2017)
6. Kin Fai Mak, Changgu Lee, James Hone, Jie Shan & Tony F. Heinz, Atomically Thin MoS₂: A New Direct-Gap Semiconductor, *Phys. Rev. Lett.* **105**, 136805 (2010).
7. Wang, Q. H., Kalantar-Zadeh, K., Kis, A., Coleman, J. N. & Strano, M. S. Electronics and optoelectronics of two-dimensional transition metal dichalcogenides. *Nature Nanotech.* **7**, 699–712 (2012).
8. Kin Fai Mak and Jie Shan, Photonics and optoelectronics of 2D semiconductor transition metal dichalcogenides, *Nature Photon.* **10**, 216-226 (2016)
9. Siddharth Sampat *et al.* Exciton and Trion Energy Transfer from Giant Semiconductor Nanocrystals to MoS₂ Monolayers. *ACS Photonics* **3**, 708–715 (2016).
10. Ross, J. S. *et al.* Electrical control of neutral and charged excitons in a monolayer semiconductor. *Nat. Commun.* **4**, 1474 (2013).
11. Kin Fai Mak, Di Xiao & Jie Shan, Light–valley interactions in 2D semiconductors, *Nature Photon.* **12**, 451-460 (2018)
12. Meng-Lin Tsai *et al.*, Monolayer MoS₂ Heterojunction Solar Cells. *ACS nano*, **8**, 8317-8322 (2014)
13. Eric Singh, Ki Seok Kim, Geun Young Yeom, & Hari Singh Nalwa, Atomically Thin-Layered Molybdenum Disulfide (MoS₂) for Bulk-Heterojunction Solar Cells, *ACS Appl. Mater. Interfaces*, **9**, 3223-3245 (2017)
14. Long Yuan, Ti Wang, Tong Zhu, Mingwei Zhou, & Libai Huang, Exciton Dynamics, Transport, and Annihilation in Atomically Thin Two-Dimensional Semiconductors, *J. Phys. Chem. Lett.* **8**, 3371–3379 (2017)
15. Yasunari Tamai, Hideo Ohkita, Hiroaki Bente & Shinzaburo Ito, Exciton diffusion in conjugated polymers: from fundamental understanding to improvement in photovoltaic conversion efficiency. *J. phys. Chem. Lett.* **6**, 3417-3428 (2015).
16. Menke S. Matthew, Wade A. Luhman & Russell J. Holmes. Tailored exciton diffusion in organic photovoltaic cells for enhanced power conversion efficiency. *Nature Mater.* **12**, 152-157 (2013).
17. Lin Jason D. A., *et al.* Systematic study of exciton diffusion length in organic semiconductors by six experimental methods. *Mater. Horiz.* **1**, 280-285 (2014).
18. Pendry J. B., Negative Refraction Makes a Perfect Lens. *Phys. Rev. Lett.*, **85**, 3966-3969 (2000).

19. Ruben Maas, James Parsons, Nader Engheta & Albert Polman, Experimental realization of an epsilon-near-zero metamaterial at visible wavelengths, *Nature Photon.* **7**, 907, (2013)
20. Nanfang Yu & Federico Capasso, Flat optics with designer metasurfaces, *Nature Mater.* **13**, 139 (2014)
21. Esfandyarpour, M., Garnett, E. C., Cui, Y., McGehee, M. D. & Brongersma, M. L., Metamaterial mirrors in optoelectronic devices, *Nature Nanotech.* **9**, 542-547 (2014).
22. Hyosung Choi *et al.* Versatile surface plasmon resonance of carbon-dot-supported silver nanoparticles in polymer optoelectronic devices, *Nature Photon.* **7**, 732-738 (2013)
23. Hossein Hodaei *et al.* Enhanced sensitivity at higher-order exceptional points, *Nature*, **548**, 187–191 (2017)
24. Jacob B. Khurgin & Greg Sun, Comparative analysis of spasers, vertical-cavity surface-emitting lasers and surface-plasmon-emitting diodes, *Nature Photon.* **8**, 468–473 (2014)
25. R. Zhang *et al.* Chemical mapping of a single molecule by plasmon-enhanced Raman scattering, *Nature* **498**, 82-86 (2013)
26. Harish N. S. Krishnamoorthy, Zubin Jacob, Evgenii Narimanov, Ilona Kretzschmar & Vinod M. Menon, Topological Transitions in Metamaterials, *Science* **336**, 205-209 (2012)
27. Alexander Poddubny, Ivan Iorsh, Pavel Belov & Yuri Kivshar, Hyperbolic metamaterials, *Nature Photon.* **7**, 958-967 (2013)
28. Dylan Lu, Jimmy J. Kan, Eric E. Fullerton & Zhaowei Liu, Enhancing spontaneous emission rates of molecules using nanopatterned multilayer hyperbolic metamaterials, *Nature Nanotech.* **9**, 48-53 (2014)
29. Tumkur T., Zhu G., Black P., Barnakov Yu. A., Bonner C. E., & Noginov M. A., Control of spontaneous emission in a volume of functionalized hyperbolic metamaterial, *Appl. Phys. Lett.* **99**, 151115 (2011)
30. Kwang Jin Lee, Yeon Ui Lee, Sang Jun Kim & Pascal André, Hyperbolic dispersion dominant regime identified through spontaneous emission variations near metamaterial interfaces, *Adv. Mater. Interfaces* **5**, 1701629 (2018)
31. Kwang Jin Lee *et al.* Charge-transfer dynamics and nonlocal dielectric permittivity tuned with metamaterial structures as solvent analogues, *Nature Mater.* **16**, 722-730 (2017)
32. Kwang Jin Lee *et al.* Blue-Shifting intramolecular charge transfer emission by nonlocal effect of hyperbolic metamaterials, *Nano Lett.* **18**, 1476-1482 (2018)
33. Shrouq H. Aleithan, *et al.* Broadband femtosecond transient absorption spectroscopy for a CVD MoS₂ monolayer, *Phys. Rev. B* **94**, 035445 (2016).
34. A. Carvalho, R. M. Ribeiro & A. H. Castro Neto, Band nesting and the optical response of two-dimensional semiconducting transition metal dichalcogenides, *Phys. Rev. B* **88**, 115205, (2013)
35. Daichi Kozawa *et al.* Photocarrier relaxation pathway in two-dimensional semiconducting transition metal dichalcogenides, *Nature Commun.* **5**, 4543, (2014)
36. Lei Wang *et al.* Slow cooling and efficient extraction of C-exciton hot carriers in MoS₂ monolayer, *Nature Commun.* **8**, 13906 (2016)
37. Daichi Kozawa *et al.* Photocarrier relaxation pathway in two-dimensional semiconducting transition metal dichalcogenides, *Nature Commun.* **5**, 4543 (2014)
38. Dezheng Sun *et al.* Observation of Rapid Exciton–Exciton Annihilation in Monolayer Molybdenum Disulfide, *Nano Lett.* **14**, 5625-5629 (2014).
39. Nardeep Kumar, Qiannan Cui, Frank Ceballos, Dawei He, Yongsheng Wang & Hui Zhao, Exciton-exciton annihilation in MoSe₂ monolayers, *Phys. Rev. B* **89**, 125427 (2014)
40. Long Yuan & Libai Huang, Exciton dynamics and annihilation in WS₂ 2D semiconductors, *Nanoscale* **7**, 7402-7408, (2015)
41. Cristian L. Cortes & Zubin Jacob, Fundamental figures of merit for engineering Förster resonance energy transfer, *Opt. Express* **26**, 19371-19387 (2018)
42. E. Engel, K. Leo & M. Hoffmann, Ultrafast relaxation and exciton–exciton annihilation in PTCDA thin films at high excitation densities, *Chem. Phys.* **325**, 170–177 (2006).
43. H.-Y. Shin *et al.* Exciton diffusion in near-infrared absorbing solution-processed organic thin films, *Phys. Chem. Chem. Phys.* **15**, 2867-2872 (2013)
44. R. C. Powell & Z. G. Soos, Kinetic Models for Energy Transfer, *Phys. Rev. B* **5**, 1547 (1972).

Acknowledgments

This research was supported by Bill & Melinda Gates Foundation, National Science Foundation, and National Natural Science Foundation (NSFC, Grant Nos. 11804334).

Additional Information

Author contributions

K.J.L. and C.G conceived and designed the experiments. K.J.L. carried out the transient absorption measurements and analyzed the entire data and wrote the manuscript. X.M., F. X., and J. L. prepared MoS₂ monolayers. W.X. prepared MoS₂-HMM hybrid structures and characterized the entire samples. C.H., J.Z., and M.E. prepared and characterized metamaterials samples. C.G. supervised whole project. All authors commented the manuscript.

Competing Financial Interests

The authors declare no competing financial interests.

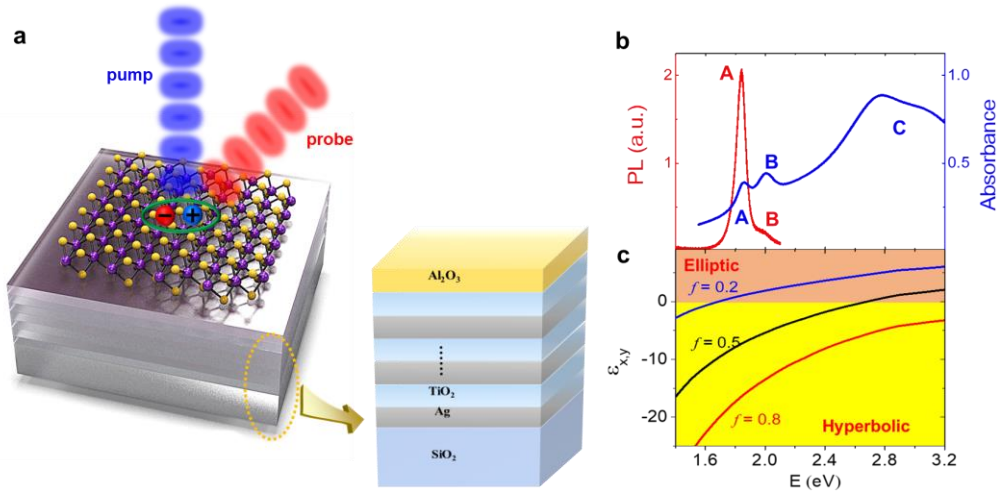


Figure 1. Sample configuration and characterization. **a**, Schematics of the experimental configuration for a MoS₂ monolayer with exciton dynamics based on the transient absorption measurements. The MoS₂ monolayer is deposited on a multilayered HMM structure that consists of 5 pairs of Ag-TiO₂ layers covered by a Al₂O₃ film to block any charge transport **b**, Absorption and photoluminescence spectra of MoS₂ monolayers with A-,B- and C-excitons. **c**, the Real part of the transverse effective dielectric function of HMM for three different fill factors ($f=0.2, 0.5, 0.8$)

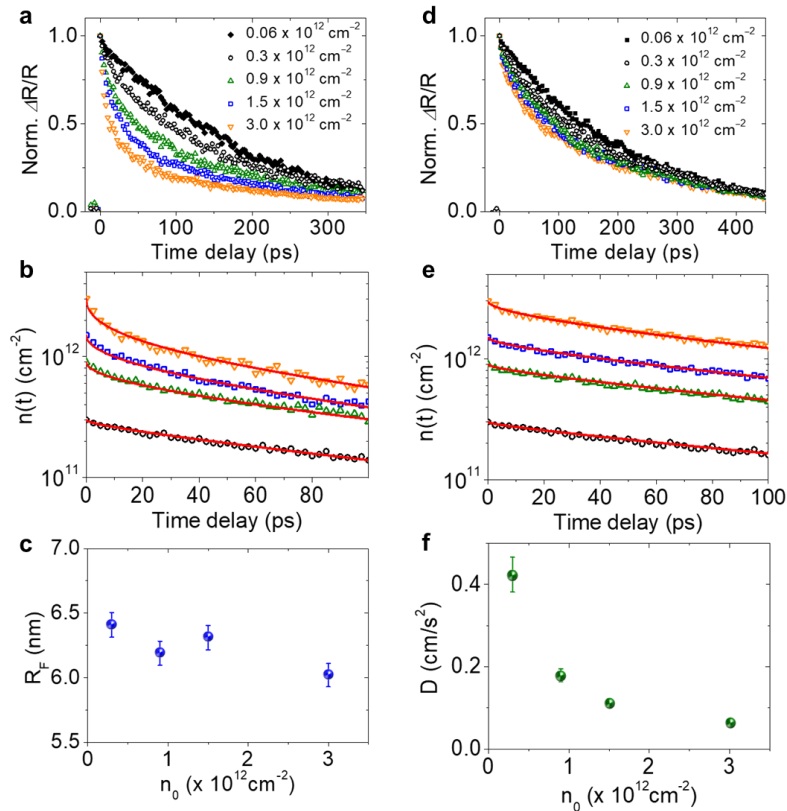


Figure 2. Transient absorption decays and fitting curves based on exciton-exciton annihilation. **a-c**: A-excitons, **d-f**: C-excitons. **a,d**, Normalized transient absorption decay of A- and C-excitons respectively for several initial exciton densities. **b,e**, Exciton decays for A- and C-excitons respectively in the initial time range (up to 100 ps) with fitting curves based on Eq. (2). **c, f**, the Forster radii and the diffusion constants for A- and C-excitons with initial exciton density n_0 .

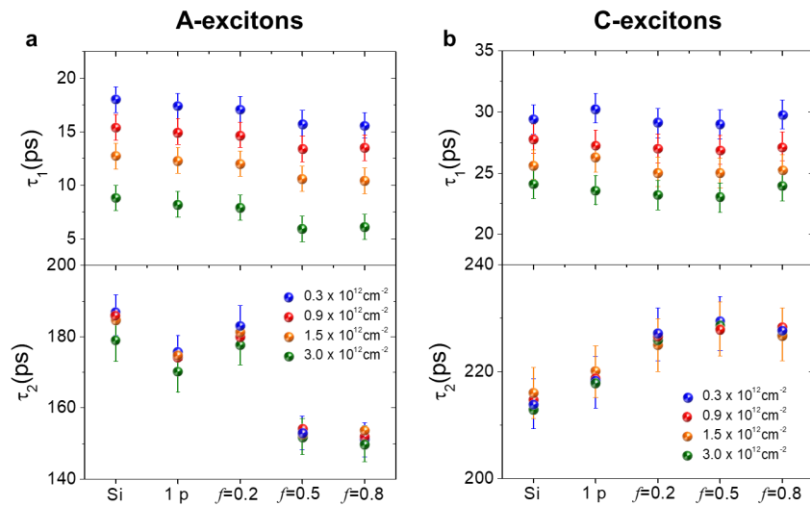


Figure 3. Behaviors of time constants for A- and C-excitons with different substrates **a**, Short (τ_1) and long (τ_2) characteristic time constants of A-excitons with different substrates for several initial exciton densities. **b**, Short (τ_1) and long (τ_2) characteristic time constants of C-excitons with different substrates for several initial exciton densities.

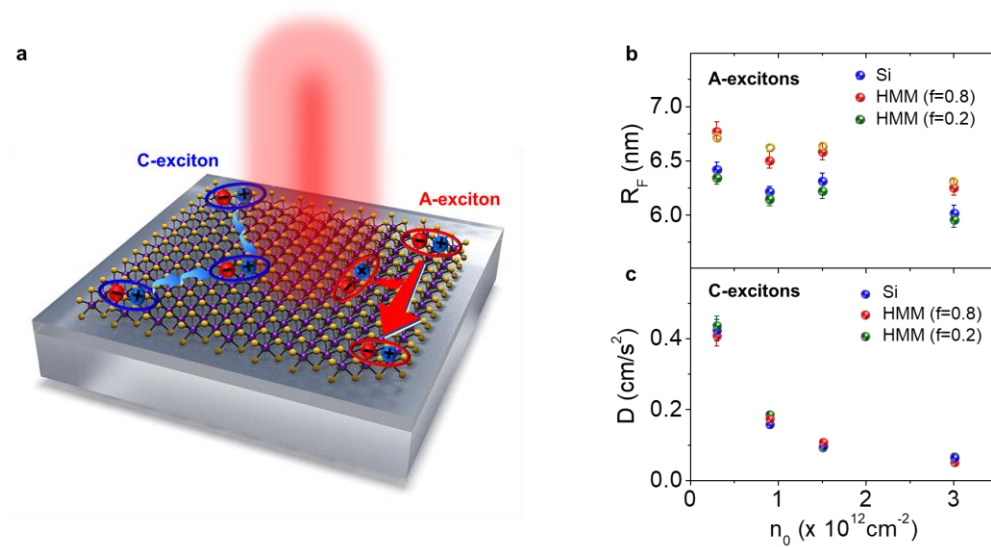


Figure 4. Underlying mechanism for exciton dynamics and behaviors of the Förster radius and diffusion constant **a**, Schematics shows the different migration mechanisms for A- and C-excitons **b**, Förster radius and **c**, the Diffusion constants for A- and C-excitons as a function of the initial exciton density on different substrates (Si, HMM with $f=0.2$ and 0.8). The overall measured behaviors for $f=0.5$ are almost identical to those for $f=0.8$.